Binding of Thioflavin T and Related Probes to Polymorphic Models of Amyloid-β Fibrils

Francesca Peccati,*,† Stefano Pantaleone,† Vanessa Riffet,‡,¶ Xavier Solans-Monfort,† Julia Contreras-García,‡ Victor Guallar,§,‖ and Mariona Sodupe†,‖

†*Departament de Química, Universitat Autònoma de Barcelona, 08193 Bellaterra, Spain* ‡*Sorbonne Universités, UPMC Univ Paris 06, CNRS, Laboratoire de Chimie Théorique (LCT), 4 place Jussieu F-75005 Paris, France*

¶*Institut Photovoltaïque d'Ile de France (IPVF), 8 rue de la Renaissance 92160 Antony, France and Institute for Research and Development of Photovoltaic Energy (IRDEP), UMR 7174 CNRS / EDF R&D / Chimie ParisTech-PSL, 6 quai Watier, 78401 Chatou, France*

§*Joint Barcelona Supercomputing Center - Centre for Genomic Regulation - Institute for Research in Biomedicine - Research Program in Computational Biology, Barcelona Supercomputing Center, Barcelona, Spain*

‖*ICREA, Passeig Lluís Companys 23, E-08010 Barcelona, Spain*

E-mail: francesca.peccati@uab.cat

Abstract

Alzheimer's disease is a challenge of the utmost importance for contemporary society. An early diagnosis is essential for the development of treatments and for establishing a network of support for the patient. In this light the deposition in the brain of amyloid-β fibrillar aggregates, which is a distinctive feature of Alzheimer, is key for an early detection of this disease. In this work we propose an atomistic study of the

interaction of amyloid tracers with recently published polymorphic models of amyloid-β 1-40 and 1-42 fibrils, highlighting the relationship between marker architectures and binding affinity. This work uncovers the importance of quaternary structure, and in particular of junctions between amyloid-β protofilaments, as the key areas for marker binding.

Introduction

Alzheimer's disease, the most common form of dementia, is gaining increasing attention owing to the rapid population ageing of contemporary societies.[1] One of the main hallmarks of this disease is the deposition in the brain of aggregates of the amyloid-β (Aβ) peptide, which appears to be linked to the neurological symptoms. Alzheimer's is a complex and multifactorial disease, for which a variety of hypotheses have been developed.[2–5] According to the *amyloid cascade hypothesis*, it is an unbalance between the production and clearance of Aβ which triggers the onset of the disease, making the deposition of amyloid aggregates the central event of this condition.[3] The great interest devoted to the so-called amyloidogenic proteins does not originate only from their involvement in neurodegenerative diseases, including Alzheimer's and Parkinson's, but also in heart diseases and type II diabetes.[6–9] For this reason, there is a common interest in the development of fast and safe techniques that allow the detection of Aβ aggregates in living patients, aimed at following the evolution of the disease and testing the effectiveness of experimental treatment. In this light, detailed knowledge of the interaction of probes with amyloid fibrils at the atomic level is crucial.

Amyloids are filamentous protein aggregates with a high β-sheet content. The process of amyloid formation, *amyloidogenesis*, involves the amyloidogenic proteins and consists of the aggregation of peptides and/or unstructured proteins leading to the formation of oligomers, which are partially structured, and develops into the deposition of ordered fibrils characterized by a cross-β structure. This is composed of pleated β-sheets in an arrangement which is roughly parallel to the growth direction of the fibril, and is key for amyloid detection.

The study of amyloid-β deposits, such as those involved in Alzheimer's disease, is complex. This is in part due to the extreme difficulty in obtaining high resolution structures of these fibrils, which is a direct consequence of their intrinsic polymorphism.[10–12] Owing to the combination of multiple techniques, solid state NMR spectroscopy among them, the last years have seen a significant development in this field, with the publication of a number of Aβ40 and Aβ42 models.[13–18]

At the same time, the last years have seen significant advances in the design and testing of markers for the detection of Aβ deposits in Alzheimer's disease patients. While positron emission tomography (PET) is the leading technique for amyloid identification *in vivo*, fluorescence imaging is emerging as a cheap and safe alternative.[19] The reference probes for these two techniques are Pittsburgh compound B (PiB) and Thioflavin T (ThT) respectively, which share a similar aromatic rod-like structure (Scheme 1), with PiB being designed as a neutral derivative of ThT.[20,21]

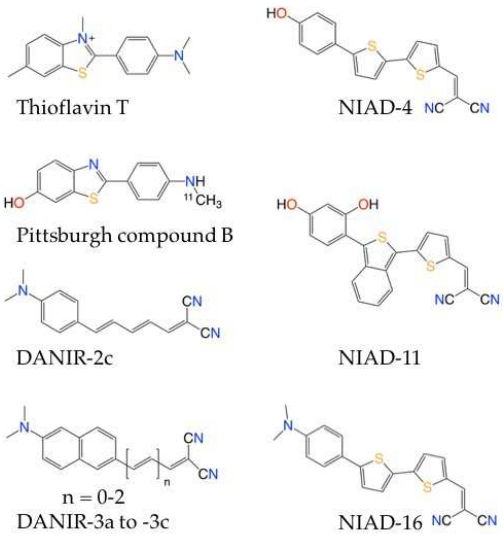

Scheme 1

Since the first observation of its amyloid staining properties (1959), ThT has been the reference for the *in vitro* staining of amyloid-β deposits. The low emission wavelength and charged character of ThT, however, prevent its application in *in vivo* conditions. For this reason, the development of fluorescence imaging for Alzheimer's disease has seen a lively

debate focused on the design of markers capable of outclassing ThT's performance.[19,22–27]

On the other hand, the fundamental mechanism of ThT binding to amyloid fibrils has been discussed for over a decade, and there is consensus on the finding that, owing to its partially rigid and rod-like architecture, ThT binds parallel to the fibril's long axis, surrounded on both sides by the regular repetition of side chains arising from the β-sheet architecture. Concisely, it can be said that ThT and the related neutral PiB selectively bind to hydrophobic and aromatic surface grooves of β-sheets, resulting in an interaction that is dominated by dispersion forces.[28–36] These studies, however, are mainly based on single protofilament models of Aβ fibrils, which were the only structures available until very few years ago.[13–15] The growing availability of fibril models opens the debate on whether small ligands, such as ThT and PiB, bind to the same aminoacidic sequences across different fibril morphologies, or if on the contrary tertiary and quaternary structure modifications can change the preferred binding poses. Furthermore, the resolution of quaternary structure reveals the structural features of areas located at the junction of two or more protofilaments, which may as well be involved in the binding of small molecules.

Tackling the complex problem of Aβ fibril-marker interactions requires a multidisciplinary approach, and computational techniques can provide atomistic insight on the nature of the binding, which is the focus of this work.

Methodology

Fibril models and markers

Since single-protofilament models such as that of Lührs et al.[14] have been extensively studied computationally, here we focus on multiple-protofilament ones. In particular, four different models of Aβ fibrils have been taken into account here: the three Aβ40 models proposed by Tycko and coworkers (Figure 1a, 1b and 1c) and the *in vitro* Aβ42 fibril model proposed independently by the groups of Riek and Griffin (Figure 1d). Binding of small molecules to

Aβ42 fibrils is particularly significant because, owing to its higher aggregation propensity, the less abundant Aβ42 represents approximately 90% of the amyloid plaques observed in Alzheimer's disease patients.[13,15–18,37] This difference in solubility between the two most common forms of Aβ peptide has been extensively studied and shown to be related to neurotoxicity, with Aβ42 being more toxic than Aβ40, and to the structure of both soluble and insoluble aggregation products.[38–41]

Models I, II and IV were obtained *in vitro* from synthetic Aβ, while model III was grown from a seed extracted from Alzheimer's disease brain tissue. These models were chosen as they represent the best approximation available of real amyloid-β deposits. Despite the evident structural diversity of the structures reported in Figure 1, the common trait of the cross-β spine, consisting of a double β-sheet zipped by complementary non-polar residues (white), is present in all models, and constitutes the protofilament of the fibril.[42] The quaternary organization of protofilaments yields its full three-dimensional structure.

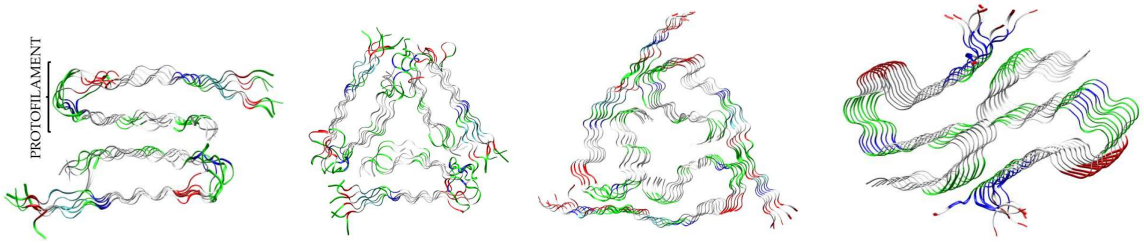

(a) Model I. (b) Model II. (c) Model III. (d) Model IV.

Figure 1: a,[13] b,[15] c[16] Models of Aβ40 and d[17,18] of Aβ42 considered in this work. Red: acidic residues, blue: basic, green: polar, white: nonpolar.

Concerning amyloid markers, we have focused on the conjugated π systems of the DANIR family[23,24,43] and on the bithiophene derivatives of the NIAD family (Scheme 1).[19,22,44,45] These markers can be considered ThT derivatives because they share a similar aromatic/conjugated linear structure, but unlike ThT they are neutral, and thus more likely to cross the blood-brain barrier. Additionally, they show improved optical properties, with the emission wavelength pushed towards the near-infrared region, which is of interest for amyloid detection *in vivo*. Despite the success of these markers, their binding to Aβ fibrils, which is an important

factor in their overall performance, is unknown.

The methodology employed in this work involves three steps. In the first step the binding poses of markers on the models of Aβ fibrils are predicted with an induced fit docking technique. In the second step molecular dynamics simulations are performed on the best ranked binding poses resulting from the docking procedure, and in the third step these dynamics simulations are used to estimate the binding energy with the MM/P(G)BSA method.[46,47] This is not dissimilar to the methodology employed in a recent work of Murugan et al.,[36] who perfomed a similar analysis on PET amyloid tracers, using Aβ40 fibril models I and II proposed by Tycko, and a single-protofilament model of Aβ42.[13–15]

Binding site search

The binding poses of the markers on the four models of Aβ fibrils were predicted using the Protein Energy Landscape Exploration (PELE) web server.[48,49] This program explores the protein energy landscape combining a Monte Carlo stochastic approach with protein structure prediction algorithms. In studies of *ligand induced fit*, such as the ones reported here, the procedure starts with an initial perturbation of the system, involving the translation and rotation of the ligand, and a normal mode displacement of the receptor's backbone. This is followed by a side chain sampling and a minimization with the OPLS (Optimized Potentials for Liquid Simulations) force field. Solvation effects are accounted for with the implicit Generalized Born Surface Area method.[50,51] These steps compose a move, corresponding to a new minimum, which is accepted or rejected based on a Metropolis criterion. In this way, each processor generates a trajectory where each minimum, candidate pose, can be ranked by its protein-ligand interaction energy. For each fibril/marker pairs, at least 45 trajectories were run, each one yielding roughly 200 minima. The quality of these predictions was tested by performing PBE-D2/6-31+G(d,p) single point interaction energy calculations on cluster models cut from selected marker/fibril models with the program Gaussian09, revision D.01.[52–55] These results are reported in detail in the ESI, and show a good agreement between

PELE and DFT (Density Functional Theory) in the energy ranking of biding poses.

Molecular dynamics simulations

Molecular dynamics simulations on selected poses were carried out with the aim of computing binding energies within the MM/P(G)BSA framework. The Amber16 package was employed with the Amber ff14SB force field. Ligand parameters were constructed using the GAFF force field and charges computed with the Restrained Electrostatic Potential (RESP) method.[56–58] For each selected PELE structure, after 2000 minimization steps, a 50 ps NVT dynamics was performed rising the temperature from 0 to 50 K with a 4 $kcal\,mol^{-1}$ restraint on the backbone of the protein, to avoid strong deformation (see ESI). A second equilibration step was performed in the NPT ensemble, of 1000 ps, with the temperature raising from 50 to 310 K in the first half of the simulation, and constant at 310 K for the second half of the simulation, with a 2 $kcal\,mol^{-1}$ restraint on the backbone. The production run involved 5 independent NPT 300 ps trajectories, with the Langevin thermostat and Monte Carlo barostat.

Binding energy evaluation

20 geometries were evenly sampled from the last 200 ps of each trajectory of the production run, and resulting 100 structures were used for binding free energy calculations neglecting the entropy term. This contribution, which has been calculated for one binding pose ($T\Delta S$= -17 $kcal\,mol^{-1}$ at T=298.15 K), has been shown by Murugan et al.[36] to be fairly constant across binding poses and markers, and thus is not expected to affect the energy ranking. It has been shown that the independent trajectories approach provides results that are more converged than those obtained from a single longer simulation.[59] The free energy values were computed on the ligand/fibril complex trajectory. In both PBSA and GBSA calculations, a ionic strength of 100 mM, which is compatible with that of a biological buffer, was employed.[57] GBSA calculations were performed with the adaptation of the generalized

Born approximation devised by Onufriev, Bashford and Case.[46,47] PBSA calculations were performed using the internal PBSA solver of Amber.[57]

Non-covalent interactions analysis

Binding of fluorescent and PET probes to amyloid fibrils involves non-covalent interactions. In this light, analysis of such interactions can aid unravel the nature of the binding. For selected binding poses, non-covalent interactions were analyzed with the NCIPLOT program, according to the methodology developed by Yang and coworkers.[60,61] The reduced density gradient $s(\boldsymbol{r})$ (eq. 1) is plotted against the electron density $\rho(\boldsymbol{r})$ multiplied by the sign of the second eigenvalue of the density Hessian.

$$s(\boldsymbol{r}) = \frac{1}{2(3\pi^2)^{1/3}} \frac{|\nabla\rho|}{\rho^{4/3}} \tag{1}$$

The low density and low gradient regions of these plots carry information on the weak (non-covalent) interactions of the system, with negative contributions being bonding and positive ones non-bonding (repulsive).

Results and discussion

Binding site search

PELE simulations yielded a large number of protein-ligand minima, from which several binding poses can be extracted for each fibril/marker pair. For clarity's sake, this manuscript focuses on a small subset of theses poses, those common to all markers and ranked best by PELE and the associated DFT-D calculations, while the rest are reported extensively in the ESI. Binding poses are named according to the position occupied by the marker on fibrils as follows: ji: junction-internal, je: junction-external, jc: junction-corner and pi: protofilament-internal. In general, our PELE simulations predict that all markers tend to interact with the

same motifs of the fibril models. The most common binding pockets on the four models of amyloid-β fibrils are reported in Figure 2. Concerning model I, the most favorable interaction corresponds to binding pose I-ji (Figure 2a), in which the marker is accommodated at the center of the fibril, at the junction between the two protofilaments. In this region, markers are in contact with residues GLY33 and MET35, which form a cavity. A second interaction that has been observed for all markers is the one reported in Figure 2b. In this case, the molecule is again located at the junction between the two protofilaments, but in an external position. The binding involves the residues located at the turn of cross-β unit of the first protofilament, namely ASN27, GLY29 and ILE31. Concerning the second protofilament, the C-terminal residues of VAL40 and GLY37 are the closest ones to the marker. While for I-ji the ligand is buried deep in the hydrophobic core and completely shielded from the solvent, in I-je the molecule is partially exposed.

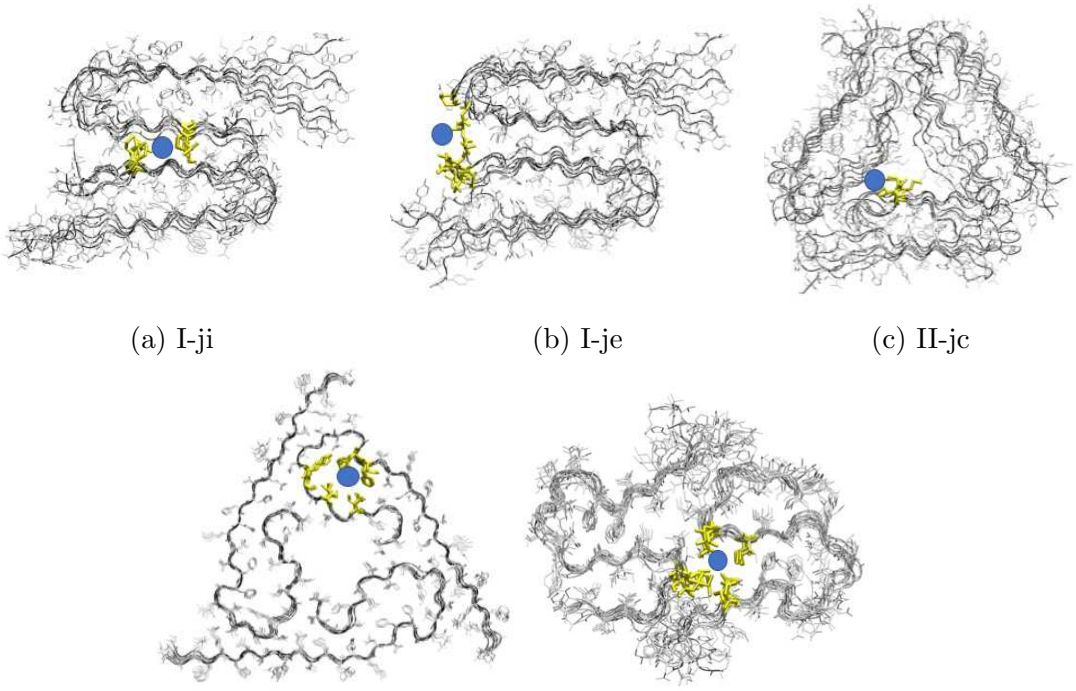

(a) I-ji (b) I-je (c) II-jc

(d) III-pi (e) IV-ji

Figure 2: Most common marker binding regions of fibril models a and b I, c II, d III and e IV. ji: junction-internal, je: junction-external, pi: protofilament-internal and jc: junction-corner. Residues involved in the interaction: I-ji: GLY33, MET35; I-je: ASN27, GLY29, ILE31, GLY37, VAL40; II-jc: MET35; III-pi: PHE19, PHE20, ILE31, LEU34; IV-ji: LEU17, ILE 32, LEU 34, MET35.

Concerning fibril model II, our simulations showed that markers are preferentially accommodated at any of the three corners defined by the triangular shaped central cavity of the fibrils (Figure 2c). In this pose, the probe once again interacts with the non-polar chains of MET35, which partially shield the ligand from the solvent. Owing to the 3-fold symmetry of fibril II, the three corners are equivalent (see ESI). Although also model III has a three fold symmmetry, with MET35 residues located at the corners of the internal, triangular shaped, cavity, for this model the favorite pose involves the binding of the probe within an internal cavity that is defined by a single protofilament (Figure 2d). This pocket is defined mainly by hydrophobic residues, namely PHE19, PHE20, LYS28, GLY29, ILE31 and LEU34.

Regarding the model of Aβ42 fibril, probes again interact preferentially with the hydrophobic portion of the structure at the junction between the two S-shaped protofilaments

(Figure 2e). Here, residues LEU17, ILE32 and LEU34 of one protofilament and MET35 of the other surround the marker. Further details about the binding modes are reported in the next section, but it is worth mentioning that all these pockets share a channel-like geometry arising from the regular repetition of side chains that is typical of the cross-β motif, and which matches the linear, rod-like, architecture of the markers.

Binding free energies

The binding free energies computed with MM/P(G)BSA corresponding to these poses are reported in Table 1, along with the decomposition into van der Waals (vdW) and electrostatic (el) contributions and the difference between the solvation free energies of the ligand-receptor complex and the two separate components.

Table 1: MM/PBSA binding energies in $kcal\,mol^{-1}$. $\Delta G_{b,PBSA}$: PBSA binding free energy in solution; $\Delta\Delta G_{s,PBSA}$=$\Delta G_{solv}(RL) - \Delta G_{solv}(R) - \Delta G_{solv}(L)$ in the PBSA framework, where R is the receptor and L the ligand. This corresponds to the difference between the solvation energy ΔG_{solv} of the ligand-receptor complex (RL) and the solvation energies of the two separate components. $\Delta G_{b,GBSA}$: GBSA binding free energy in solution; el: electrostatic and vdW: dispersion contributions to the binding energy *in vacuo*; $\Delta\Delta G_{s,GBSA}$=$\Delta G_{solv}(RL) - \Delta G_{solv}(R) - \Delta G_{solv}(L)$ in the GBSA framework. Average error: $\pm$ 2-5 $kcal\,mol^{-1}$, computed as the standard deviation divided by the square root of the number of frames.

	$\Delta G_{b,PBSA}$	$\Delta\Delta G_{s,PBSA}$	vdW	el	$\Delta G_{b,GBSA}$	$\Delta\Delta G_{s,GBSA}$		$\Delta G_{b,PBSA}$	$\Delta\Delta G_{s,PBSA}$	vdW	el	$\Delta G_{b,GBSA}$	$\Delta\Delta G_{s,GBSA}$
I-ji							III-pi						
ThT	-13.3	258.8	-49.7	-222.3	-26.6	245.5	ThT	-27.9	733.1	-48.2	-712.9	-37.6	723.4
PiB	-8.9	48.6	-52.0	-5.6	-47.0	10.6	PiB	-2.6	46.2	-39.6	-9.2	-35.3	13.5
DANIR-2c	-16.2	51.6	-51.5	-16.3	-50.4	17.4	DANIR-2c	-9.7	42.1	-45.3	-6.5	-41.8	10.0
DANIR-3a	-9.1	53.8	-51.0	-12.0	-42.9	10.0	DANIR-3a	-11.8	52.5	-47.6	-16.7	-45.0	19.3
DANIR-3b	-15.6	59.2	-58.5	-16.3	-52.6	22.2	DANIR-3b	-13.0	43.6	-47.2	-9.4	-41.1	15.5
DANIR-3c	-16.1	64.3	-64.7	-15.6	-56.4	24.0	DANIR-3c	-12.0	49.3	-50.4	-11.0	-44.6	16.7
NIAD-4	-13.5	62.2	-63.0	-12.8	-55.5	20.3	NIAD-4	-10.6	61.6	-52.8	-19.4	-47.9	24.2
NIAD-11	-10.7	67.2	-60.5	-17.4	-48.2	29.7	NIAD-11	1.9	84.0	-51.1	-31.0	-47.0	35.2
NIAD-16	-19.4	66.1	-69.8	-15.7	-63.5	21.9	NIAD-16	-9.8	40.3	-55.5	5.4	-51.0	-0.9
I-je							IV-ji						
ThT	0.1	292.0	-28.4	-263.6	-15.2	276.8	ThT	-7.1	178.2	-48.0	-137.3	-15.0	170.2
PiB	5.9	30.6	-20.5	-4.2	-11.4	13.3	PiB	-9.8	40.4	-38.0	-12.2	-31.3	18.9
DANIR-2c	0.2	34.0	-37.2	3.3	-28.5	5.4	DANIR-2c	-8.6	41.6	-45.0	-5.2	-40.7	9.4
DANIR-3a	-1.1	34.2	-32.8	-2.4	-23.0	12.3	DANIR-3a	-11.6	42.5	-45.9	-8.2	-36.7	17.4
DANIR-3b	-2.0	43.1	-41.6	-3.4	-31.4	13.6	DANIR-3b	-8.4	41.3	-45.9	-3.8	-38.1	11.6
DANIR-3c	2.2	49.7	-36.8	-10.7	-24.0	23.4	DANIR-3c	-11.2	50.3	-48.7	-12.8	-45.0	16.5
NIAD-4	-3.3	50.5	-46.1	-7.6	-36.5	17.2	NIAD-4	-12.0	43.1	-49.6	-5.5	-39.9	15.2
NIAD-11	7.7	53.2	-37.8	-7.7	-25.6	19.9	NIAD-11	-2.5	40.8	-31.5	-11.8	-21.8	21.5
NIAD-16	-5.7	62.6	-46.5	-21.7	-39.8	28.4	NIAD-16	-7.7	49.4	-51.4	-5.6	-41.5	15.6
II-jc													
ThT	-9.9	282.1	-45.5	-246.5	-27.6	264.4							
PiB	-5.4	61.2	-36.8	-29.8	-37.6	29.0							
DANIR-2c	-3.7	43.3	-41.2	-5.8	-35.6	11.4							
DANIR-3a	-3.7	32.1	-38.0	2.2	-29.6	6.2							
DANIR-3b	-7.0	45.0	-43.5	-8.5	-35.1	16.9							
DANIR-3c	-9.2	49.4	-51.8	-6.9	-45.5	13.2							
NIAD-4	-6.6	56.6	-49.9	-13.4	-42.6	20.6							
NIAD-11	-2.3	64.3	-46.8	-19.8	-39.0	27.6							
NIAD-16	-8.3	51.6	-51.9	-8.0	-45.9	14.0							

Contributions to the binding interaction in pose I-ji

This pose involves the interaction of markers with MET35 side chains, with a binding energy in the -9 to -19 $kcal\,mol^{-1}$ range in the PBSA framework. Energy decomposition indicates that van der Waals interactions account for roughly 80% of the binding energy (computed from the electrostatic el and van der Waals vdW terms of Table 1), which is not surprising owing to the hydrophobic nature of methionine and the aromatic structure of the markers. The remaining contribution is electrostatic, and includes the hydrogen bond contacts that may be formed between the marker and the backbone. This has been confirmed by analyzing the non-covalent interactions of the NIAD-4/I-ji system, as shown in Figure 3a. The presence of a peak in the negative region of the density multiplied by the sign of the second eigenvalue of the density Hessian axis is indicative of a single, strong, hydrogen bond, that is formed between the hydroxyl group of the marker and a carbonyl group of the backbone (Figure 3b). A second contribution, which corresponds to the lowest density values (green part of the plot), corresponds to van der Waals interactions, and is shown in Figure 3c to involve the whole aromatic body of the marker.

This result anticipates a trait that is common to all the binding poses observed: rather than involving specific residues, the binding is driven by geometric complementarity; all the presented markers, indeed, share a linear conjugated/aromatic structure with the correct dimension to fit into the hydrophobic channels arising from the cross-β structure of amyloid fibrils (Figure 3e). These channels, with diameters ranging from 10 to 13 Å, are normally delimited by hydrophobic or aromatic side chains, which explains the strong van der Waals contribution to the binding. The lack of specificity of this interaction is reflected in the binding energies, that, at least for this binding pose, are quite constant across the range of markers explored, with the exception of ThT. The electrostatic contribution to the binding of ThT is significantly larger than that of the other markers (Table 1), and is compensated by the electrostatic contribution to $\Delta\Delta G_s$ (Table 1). This originates from the charge of the marker, and is a well-known feature of MM/PBSA and GBSA calculations.[59] The two

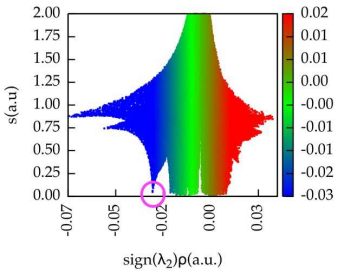

(a) NCI plot.

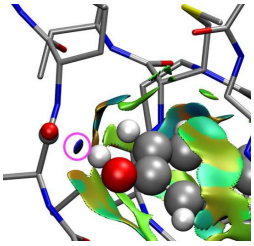

(b) H bond with the backbone.

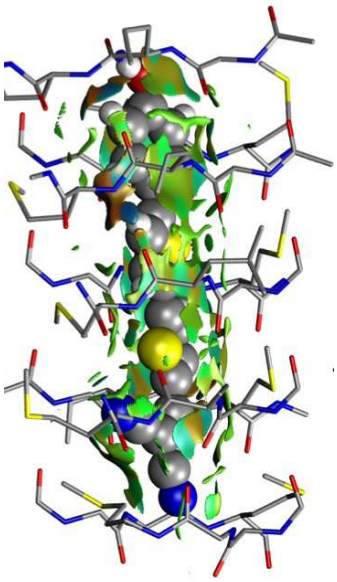

(c) van der Waals interactions.

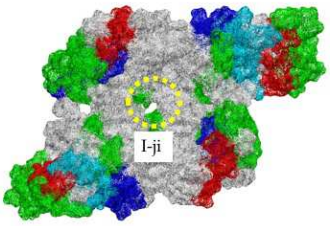

(d) Surface of fibril I.[62,63]

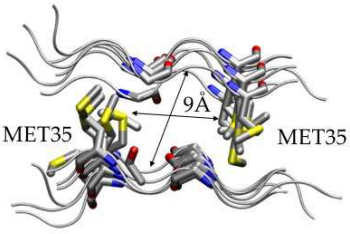

(e) Binding channel.

Figure 3: Analysis of binding pose NIAD-4/I-ji.

numbers usually cancel out, and introduce a degree of uncertainty in the binding energy result. However, the van der Waals contribution to the binding energy of ThT is essentially the same as that of PiB, its related neutral compound. This, along with the fact that ThT binds in the same motifs as the neutral markers, indicates not only that salt bridges with negatively charged residues are not necessary for the binding, as already reported by Shea and coworkers,[33] but also that the net effect of bearing a positive charge is minor.

Contributions to the binding interaction in pose I-je

Compared to the previous one, this pose is more easily accessible, as it involves binding of the small molecule to the less ordered exterior portion of the junction between the protofilaments. Owing to its less ordered nature, however, this shallow binding pocket yields a poorer stabilization, with small or even positive MM/PBSA binding energies that are still dominated by the van der Waals term. This indicates a strong preference of all markers for the solvent excluded internal portion of the fibrils. This result is in agreement with what was recently reported by Murugan et al.[36] It is worth stressing that along with these two "junction"

binding modes, both our calculations and those of Murugan et al. predicted a number of intra-protofilament binding poses, with binding energies that are comparable or smaller than that of I-ji. Detection of several binding poses common to all markers, which are described in detail in the ESI, matches the experimental observation that Aβ fibrils can accommodate a wide range of structural variations of the same molecule, and that they present a variety of binding poses corresponding to different chemical environments and binding affinities.[64–66] Therefore, interpretation of experimental binding affinities of such systems is complicated by both the conformational freedom of Aβ aggregates and the multiplicity of binding sites.[67]

Contributions to the binding interaction in pose II-jc

This binding pose represents an exception, because it is the only stable binding mode observed where the marker is not sandwitched between parallel β-sheets (Figure 4); despite the fact that also more internal binding poses have been observed (see ESI), mode II-jc is by far the most frequent binding mode. A possible explanation to its uniqueness is that in the binding cavity the marker is wrapped by the hydrophobic side chains of MET35, which effectively shield the dye from the solvent. Indeed, as in all binding poses, dispersion dominates the interaction, though to a lesser extent than for I-ji. Again, the binding pocket is shaped like a channel and involves interaction with the regular rows of side chains arising from the cross-β structure of amyloid protofilaments (Figure 4). This confirms the stability of this cavity and its likelyhood as binding pocket, as hypothesized by Miller et al.[68] Electrostatic interactions, like in previous cases, involve hydrogen bonds between hydroxyl groups of the ligands and carbonyl groups of the backbone.

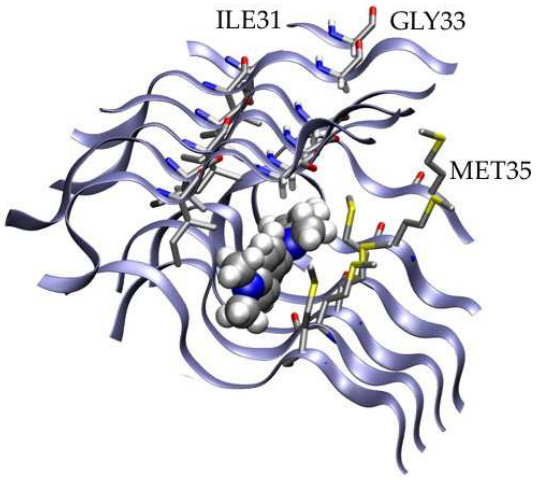

Figure 4: ThT/II-jc. Channel size: 8 × 9 Å.

Contributions to the binding interaction in pose III-pi

Fibril III shares with model II a triangular shape, but with a significant structural difference: protofilaments are arranged so that the internal β-sheet forms a turn. This turn leaves a variable distance between the parallel β-units, and a further turn in the terminal residues of each protofilament, which interacts with the loop of another. The key feature of this fibril, as far as binding of small conjugated ligands is concerned, is the variable distance between the β-sheets of each protofilament, leading to a multiplicity of hydrophobic channel-like binding pockets with a variety of sizes. A binding mode that has been observed for all markers involves binding in a relatively large channel defined by hydrophobic residues. Dyes are sandwiched between PHE19 and PHE20, whose side chains, according to the experimental model, are both oriented towards the internal, solvent excluded, portion of the fibril, and ILE31 and LEU34, resulting in a highly hydrophobic environment (Figure 5). In terms of binding energy, this translates into a 50 $kcal\,mol^{-1}$ van der Waals term, which is essentially constant across different markers. Again, markers such as PiB, bearing hydroxyl groups, can form hydrogen bonds with carbonyl groups of the backbone, which in this case belong to ILE31 and are oriented toward the interior of the binding channel. Additionally, different

binding modes were observed, involving different portions of the protofilament, and mainly hydrophobic/aromatic residues (see ESI).

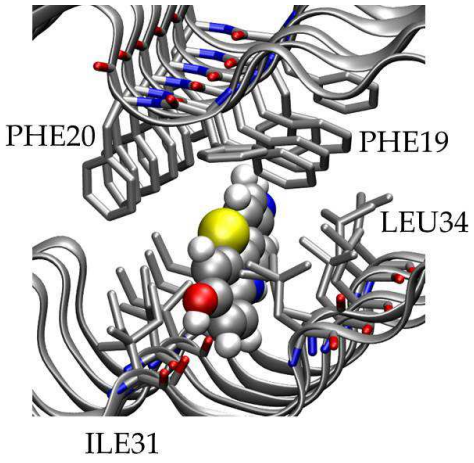

Figure 5: PiB/III-pi. Channel size: 12 × 6 Å.

Contributions to the binding interaction in pose IV-ji

The recently published Aβ42 fibril model has a two-fold symmetry, and each of the two protofilaments assumes an S-shaped conformation (Figure 6a). Intra-protofilament interactions, which are responsible for this conformation, involve a salt bridge between LYS28 and ALA42 (C-terminus) and a number of hydrophobic interactions. This is a significant difference from Aβ40 models, where the salt bridge involves LYS28 and ASP23. Inter-protofilament interactions, on the other hand, involve residues GLN15, LEU17 and MET35 (Figure 6a).[17,18] This is relevant because markers bind just in the hydrophobic channel defined by residues LEU17, ILE 32, LEU 34 and MET35, as shown in Figure 6b.

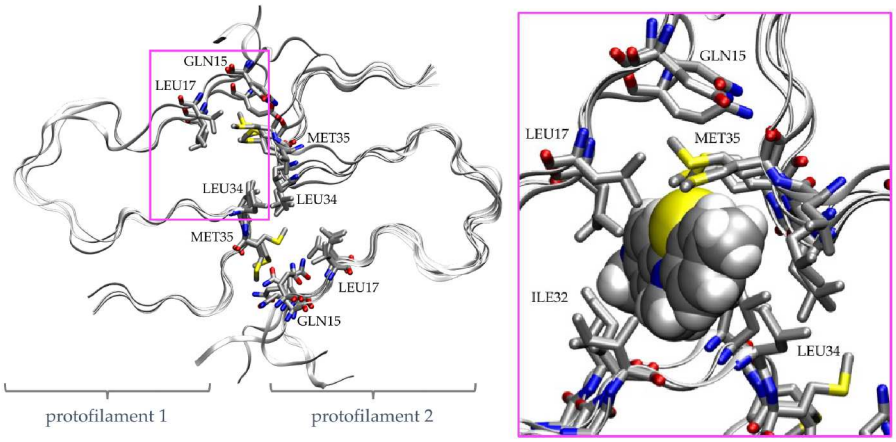

(a) Inter-protofilament interactions. (b) ThT/IV-ji.

Figure 6: Aβ42 inter-protofilament interactions and binding pocket.

This pose is similar to I-ji of Aβ40, with the markers buried in the hydrophobic zipper connecting the protofilaments. Owing to its inferior solubility compared to Aβ40, Aβ42 is more abundant in Alzheimer's plaques, and thus is particularly significant when comparing calculated binding energies with experimental ones. MM/PBSA binding energies for IV-ji are in the -8 to -12 $kcal\,mol^{-1}$ range, with the exception of ThT (-7.1) and NIAD-11 (-2.5). Binding energies of the same order of magnitude can be expected, again, because the markers share the same aromatic rod-like architecture, and in all cases dispersion dominates the binding (Table 1). Despite the error of $\sim$ 2-5 $kcal\,mol^{-1}$ on the energy, MM/PBSA calculations seem to reproduce the experimental trends: PiB shows a superior affinity ($\Delta G_{s,PBSA}$ = -9.8 $kcal\,mol^{-1}$) for Aβ than ThT ($\Delta G_{s,PBSA}$ = -7.1 $kcal\,mol^{-1}$), which is in line with the experimental values reported in Table 2 and the calculations of Shea and coworkers.[33] Indeed, the positive charge of ThT results in a higher solvation energy than the neutral compounds, and thus lower binding affinity. Moreover, DANIR-3c has a higher affinity than DANIR-2c, which can be attributed to the more extended π system, which in turn increases van der Waals interactions.

Table 2: Experimental values of binding constants. Constants from refs.[65] and[24] were obtained with fluorescence assays, those from refs.[64],[23] and[19] from radioligand binding assays.

marker	Binding affinity (nM)	type of fibril
ThT[65]	$K_d = 790 \pm 50$	Aβ40
PiB[64]	$K_d = 2.5 \pm 0.2$	AD brain
DANIR-2c[23]	$K_d = 36.9 \pm 6.8$	Aβ42
DANIR-3c[24]	$K_d = 1.9 \pm 1.1$	Aβ42
NIAD-4[19]	$K_i = 10$	Aβ40

Additionally, all fibril models yield similar ranking of binding affinities for markers of the bithiophene family (Scheme 1), with NIAD-4 and NIAD-16 involved in much stronger binding than NIAD-11. Despite similar van der Waals and electrostatic terms, NIAD-11 has to pay for its larger size, which involves closer repulsive contacts with the fibrils. A detailed analysis of the interaction showed that, owing to its size, NIAD-11 is not fully inserted between the parallel β-sheets neither in pose I-ji (Figure 7a) nor in pose IV-ji (Figure 7b). The polar portion of the molecule, bearing the two hydroxyl groups, remains exposed to the solvent. This is confirmed by the evolution of dihedral Φ (Figure 7c) along the molecular dynamics simulation. This angle, indeed, undergoes oscillations up to 50 degrees in both binding poses, indicating that its flexibility is not inferior to that of the free marker in solution, for which a separate dynamics was run.

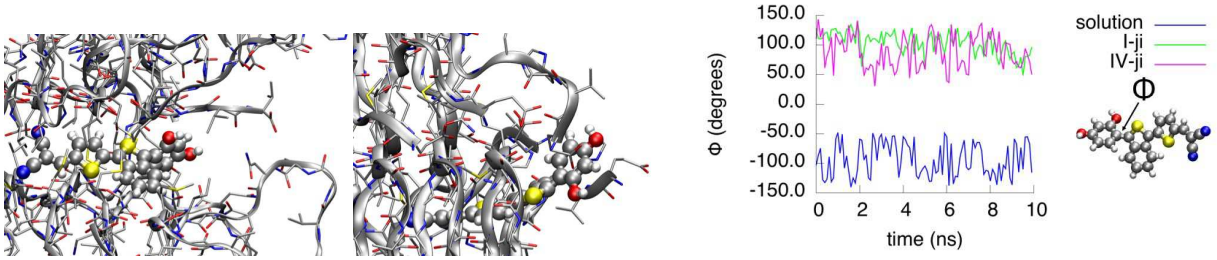

(a) I-ji (b) VI-ji (c) Dihedral Φ

Figure 7: NIAD-11 flexibility analysis from molecular dynamics simulations performed on the marker in water and bound to fibril models I and IV.

Conclusions

This systematic study of markers-Aβ fibrils binding reveals that for rod-like aromatic ligands, unspecific van der Waals interactions dominate the binding energy. In contrast to previous studies,[28–34] according to which ThT and PiB show a preference for aromatic residues at the surface grooves of Aβ fibrils, the simulations presented here highlight a preference of linear aromatic markers for the hydrophobic pockets located at the junction between protofilaments, and in particular for MET35 residues. This difference is attributed to the fact that only recently full Aβ fibril models have been published, revealing binding pockets that were not present in older single-protofilament models. This new obervation raises important questions on the relationship between ligand binding and stability of amyloid-β fibrils.

Acknowledgement

The authors gratefully acknowledge financial support from MINECO (CTQ2014-59544-P) and the Generalitat de Catalunya (2014SGR-482). F. P. and S. P. thank Universitat Autònoma de Barcelona for a predoctoral grant. M. S. gratefully acknowledges support from the ICREA Academia Award. X. S.-M. is indebted for the Professor Agregat Serra Húnter position.

Supporting Information Available

- Description of symmetry-related binding pockets;
- Information on the molecular dynamics simulations;
- DFT calculations used to calibrate the PELE induced fit docking simulations;
- Full description of all the binding poses encountered.

This material is available free of charge via the Internet at `http://pubs.acs.org/`.

References

(1) Alzheimer's Association, 2016 Alzheimer's Disease Facts and Figures. *Alzheimers Dement.* **2016**, *12*, 459–509.

(2) Terry, A. V.; Buccafusco, J. J. The Cholinergic Hypothesis of Age and Alzheimer's Disease-Related Cognitive Deficits: Recent Challenges and Their Implications for Novel Drug Development. *J. Pharm. Exp. Ther.* **2003**, *306*, 821–827.

(3) Selkoe, D. J.; Hardy, J. The Amyloid Hypothesis of Alzheimer's Disease at 25 Years. *EMBO Mol. Med.* **2016**, *8*, 595–608.

(4) Praticó, D. Oxidative Stress Sypothesis in Alzheimers Disease: a Reappraisal. *Trends Pharmacol. Sci.* **2008**, *29*, 609–615.

(5) Maccioni, R. B.; Farías, G.; Morales, I.; Navarrete, L. The Revitalized Tau Hypothesis on Alzheimer's Disease. *Arch. Med. Res.* **2010**, *41*, 226–231.

(6) Harrison, R. S.; Sharpe, P. C.; Singh, Y.; Fairlie, D. P. *Reviews of Physiology, Biochemistry and Pharmacology*; Springer Berlin Heidelberg: Berlin, Heidelberg, 2007; pp 1–77.

(7) Rapezzi, C.; Quarta, C. C.; Riva, L.; Longhi, S.; Gallelli, I.; Lorenzini, M.; Ciliberti, P.; Biagini, E.; Salvi, F.; Branzi, A. Transthyretin-Related Amyloidoses and the Heart: a Clinical Overview. *Nat. Rev. Cardiol.* **2010**, *7*, 398–408.

(8) Cooper, G. J.; Willis, A. C.; Clark, A.; Turner, R. C.; Sim, R. B.; Reid, K. B. Purification and Characterization of a Peptide from Amyloid-Rich Pancreases of Type 2 Diabetic Patients. *Proc. Natl. Acad. Sci. U.S.A.* **1987**, *84*, 8628–8632.

(9) Hardy, J.; Selkoe, D. J. The Amyloid Hypothesis of Alzheimer's Disease: Progress and Problems on the Road to Therapeutics. *Science* **2002**, *297*, 353–356.

(10) Petkova, A. T.; Leapman, R. D.; Guo, Z.; Yau, W.-M.; Mattson, M. P.; Tycko, R. Self-Propagating, Molecular-Level Polymorphism in Alzheimer's β-Amyloid Fibrils. *Science* **2005**, *307*, 262–265.

(11) Annamalai, K.; Gührs, K.-H.; Koehler, R.; Schmidt, M.; Michel, H.; Loos, C.; Gaffney, P. M.; Sigurdson, C. J.; Hegenbart, U.; Schönland, S.; *et al.*, Polymorphism of Amyloid Fibrils In Vivo. *Angew. Chem. Int. Ed.* **2016**, *55*, 4822–4825.

(12) Toyama, B. H.; Weissman, J. S. Amyloid Structure: Conformational Diversity and Consequences. *Annu. Rev. Biochem.* **2011**, *80*, 557–585.

(13) Petkova, A. T.; Yau, W.-M.; Tycko, R. Experimental Constraints on Quaternary Structure in Alzheimer's β–Amyloid Fibrils. *Biochemistry* **2006**, *45*, 498–512.

(14) Lührs, T.; Ritter, C.; Adrian, M.; Riek-Loher, D.; Bohrmann, B.; Döbeli, H.; Schubert, D.; Riek, R. 3D structure of Alzheimer's Amyloid-β(142) Fibrils. *Proc. Natl. Acad. Sci. USA* **2005**, *102*, 17342–17347.

(15) Paravastu, A. K.; Leapman, R. D.; Yau, W.-M.; Tycko, R. Molecular Structural Basis for Polymorphism in Alzheimer's β-Amyloid fibrils. *Proc. Natl. Acad. Sci. USA* **2008**, *105*, 18349–18354.

(16) Lu, J.-X.; Qiang, W.; Yau, W.-M.; Schwieters, C. D.; Meredith, S. C.; Tycko, R. Molecular Structure of β-Amyloid Fibrils in Alzheimers Disease Brain Tissue. *Cell* **2013**, *154*, 1257–1268.

(17) Colvin, M. T.; Silvers, R.; Ni, Q. Z.; Can, T. V.; Sergeyev, I.; Rosay, M.; Donovan, K. J.; Michael, B.; Wall, J.; Linse, S.; *et al.*, Atomic Resolution Structure of Monomorphic Aβ42 Amyloid Fibrils. *J. Am. Chem. Soc.* **2016**, *138*, 9663–9674.

(18) Wälti, M. A.; Ravotti, F.; Arai, H.; Glabe, C. G.; Wall, J. S.; Böckmann, A.;

Güntert, P.; Meier, B. H.; Riek, R. Atomic-Resolution Structure of a Disease-Relevant Aβ(1–42) Amyloid Fibril. *Proc. Natl. Acad. Sci. USA* **2016**, *113*, E4976–E4984.

(19) Nesterov, E. E.; Skoch, J.; Hyman, B. T.; Klunk, W. E.; Bacskai, B. J.; Swager, T. M. In Vivo Optical Imaging of Amyloid Aggregates in Brain: Design of Fluorescent Markers. *Angew. Chem. Int. Ed.* **2005**, *44*, 5452–5456.

(20) Klunk, W. E.; Wang, Y.; Huang, G.; Debnath, M. L.; Holt, D. P.; Mathis, C. A. Uncharged Thioflavin-T Derivatives Bind to Amyloid-Beta Protein with High Affinity and Readily Enter the Brain. *Life Sci.* **2001**, *69*, 1471–1484.

(21) Vassar, P.; Culling, C. Fluorescent Stains, with Special Reference to Amyloid and Connective Tissues. *Arch. Pathol.* **1959**, *68*, 487–498.

(22) Raymond, S. B.; Skoch, J.; Hills, I. D.; Nesterov, E. E.; Swager, T. M.; Bacskai, B. J. Smart Optical Probes for Near-infrared Fluorescence Imaging of Alzheimer's Disease Pathology. *Eur. J. Nucl. Med. Mol. Imaging* **2008**, *35*, 93–98.

(23) Cui, M.; Ono, M.; Watanabe, H.; Kimura, H.; Liu, B.; Saji, H. Smart Near-Infrared Fluorescence Probes with Donor-Acceptor Structure for in Vivo Detection of β-Amyloid Deposits. *J. Am. Chem. Soc.* **2014**, *136*, 3388–3394.

(24) Fu, H.; Cui, M.; Zhao, L.; Tu, P.; Zhou, K.; Dai, J.; Liu, B. Highly Sensitive Near-Infrared Fluorophores for in Vivo Detection of Amyloid-β Plaques in Alzheimers Disease. *J. Med. Chem.* **2015**, *58*, 6972–6983.

(25) Zhang, X.; Tian, Y.; Yuan, P.; Li, Y.; Yaseen, M. A.; Grutzendler, J.; Moore, A.; Ran, C. A Bifunctional Curcumin Analogue for Two-Photon Imaging and Inhibiting Crosslinking of Amyloid Beta in Alzheimer's disease. *Chem. Commun.* **2014**, *50*, 11550–11553.

(26) Zhang, X.; Tian, Y.; Li, Z.; Tian, X.; Sun, H.; Liu, H.; Moore, A.; Ran, C. Design and Synthesis of Curcumin Analogues for in Vivo Fluorescence Imaging and Inhibiting Copper-Induced Cross-Linking of Amyloid Beta Species in Alzheimers Disease. *J. Am. Chem. Soc.* **2013**, *135*, 16397–16409.

(27) Ono, M.; Watanabe, H.; Kimura, H.; Saji, H. BODIPY-Based Molecular Probe for Imaging of Cerebral β-Amyloid Plaques. *ACS Chem. Neurosci.* **2012**, *3*, 319–324.

(28) Krebs, M.; Bromley, E.; Donald, A. The Binding of Thioflavin-T to Amyloid Fibrils: Localisation and Implications. *J. Struct. Biol.* **2005**, *149*, 30–37.

(29) LeVine, H. Thioflavine T Interaction with Amyloid β-Sheet Structures. *Amyloid* **1995**, *2*, 1–6.

(30) Biancalana, M.; Makabe, K.; Koide, A.; Koide, S. Molecular Mechanism of Thioflavin-T Binding to the Surface of β-Rich Peptide Self-Assemblies. *J. Mol. Biol.* **2009**, *385*, 1052–1063.

(31) Biancalana, M.; Koide, S. Molecular Mechanism of Thioflavin-T Binding to Amyloid Fibrils. *Biochim. Biophys. Acta, Proteins Proteomics* **2010**, *1804*, 1405–1412.

(32) Groenning, M. Binding mode of Thioflavin T and Other Molecular Probes in the Context of Amyloid Fibrils - Current Status. *J. Chem. Biol.* **2010**, *3*, 1–18.

(33) Wu, C.; Bowers, M. T.; Shea, J.-E. On the Origin of the Stronger Binding of PIB over Thioflavin T to Protofibrils of the Alzheimer Amyloid-β Peptide: A Molecular Dynamics Study. *Biophys. J.* **2011**, *100*, 1316–1324.

(34) Reinke, A. A.; Gestwicki, J. E. Insight into Amyloid Structure Using Chemical Probes. *Chem. Biol. Drug. Des.* **2011**, *77*, 399–411.

(35) Wu, C.; Scott, J.; Shea, J.-E. Binding of Congo Red to Amyloid Protofibrils of the

Alzheimer Aβ(9–40) Peptide Probed by Molecular Dynamics Simulations. *Biophys. J.* **2012**, *103*, 550–557.

(36) Murugan, N. A.; Halldin, C.; Nordberg, A.; Långstram, B.; Ågren, H. The Culprit Is in the Cave: The Core Sites Explain the Binding Profiles of Amyloid-β Specific Tracers. *J. Phys. Chem. Lett.* **2016**, *7*, 3313–3321.

(37) Roher, A. E.; Lowenson, J. D.; Clarke, S.; Woods, A. S.; Cotter, R. J.; Gowing, E.; Ball, M. J. β-Amyloid-(1–42) is a Major Component of Cerebrovascular Amyloid Deposits: Implications for the Pathology of Alzheimer Disease. *Proc. Natl. Acad. Sci. USA* **1993**, *90*, 10836–10840.

(38) Schmidt, M.; Sachse, C.; Richter, W.; Xu, C.; Fndrich, M.; Grigorieff, N. Comparison of Alzheimer Aβ(140) and Aβ(142) Amyloid Fibrils Reveals Similar Protofilament Structures. *Proc. Natl. Acad. Sci. USA* **2009**, *106*, 19813–19818.

(39) Yan, Y.; Wang, C. Aβ42 is More Rigid than Aβ40 at the C Terminus: Implications for Aβ Aggregation and Toxicity. *J. Mol. Biol.* **2006**, *364*, 853–862.

(40) Chromy, B. A.; Nowak, R. J.; Lambert, M. P.; Viola, K. L.; Chang, L.; Velasco, P. T.; Jones, B. W.; Fernandez, S. J.; Lacor, P. N.; Horowitz, P.; Finch, C. E.; Krafft, G. A.; Klein, W. L. Self-Assembly of Aβ1-42 into Globular Neurotoxins. *Biochemistry* **2003**, *42*, 12749–12760.

(41) Gu, L.; Guo, Z. Alzheimer's Aβ42 and Aβ40 Peptides Form Interlaced Amyloid Fibrils. *J. Neurochem.* **2013**, *126*, 305–311.

(42) Nelson, R.; Sawaya, M. R.; Balbirnie, M.; Madsen, A. Ø.; Riekel, C.; Grothe, R.; Eisenberg, D. Structure of the Cross-β Spine of Amyloid-like Fibrils. *Nature* **2005**, *435*, 773–778.

(43) Peccati, F.; Wiśniewska, M.; Solans-Monfort, X.; Sodupe, M. Computational Study on Donor–Acceptor Optical Markers for Alzheimer's Disease: a Game of Charge Transfer and Electron delocalization. *Phys. Chem. Chem. Phys.* **2016**, *18*, 11634–11643.

(44) Peccati, F.; Hernando, J.; Blancafort, L.; Solans-Monfort, X.; Sodupe, M. Disaggregation-Induced Fluorescence Enhancement of NIAD-4 for the Optical Imaging of Amyloid-β Fibrils. *Phys. Chem. Chem. Phys.* **2015**, *17*, 19718–19725.

(45) Peccati, F.; Solans-Monfort, X.; Sodupe, M. The Role of Charge Transfer in the Photophysics of Dithiophene-Based (NIADs) Fluorescent Markers for Amyloid-β Detection. *Theor. Chem. Acc.* **2016**, *135*, 184.

(46) Onufriev, A.; Bashford, D.; Case, D. A. Exploring Protein Native States and Large-scale Conformational Changes with a Modified Generalized Born Model. *Proteins: Struct., Funct., Bioinf.* **2004**, *55*, 383–394.

(47) Onufriev, A.; Bashford, D.; Case, D. A. Modification of the Generalized Born Model Suitable for Macromolecules. *J. Phys. Chem. B* **2000**, *104*, 3712–3720.

(48) Borrelli, K. W.; Vitalis, A.; Alcantara, R.; Guallar, V. PELE: Protein Energy Landscape Exploration. A Novel Monte Carlo Based Technique. *J. Chem. Theory Comput.* **2005**, *1*, 1304–1311.

(49) Madadkar-Sobhani, A.; Guallar, V. PELE Web Server: Atomistic Study of Biomolecular Systems at Your Fingertips. *Nucleic Acids Res.* **2013**, *41*, W322–W328.

(50) Jorgensen, W. L.; Tirado-Rives, J. The OPLS [Optimized Potentials for Liquid Simulations] Potential Functions for Proteins, Energy Minimizations for Crystals of Cyclic Peptides and Crambin. *J. Am. Chem. Soc.* **1988**, *110*, 1657–1666.

(51) Kaminski, G. A.; Friesner, R. A.; Tirado-Rives, J.; Jorgensen, W. L. Evaluation and Reparametrization of the OPLS-AA Force Field for Proteins via Comparison with Ac-

curate Quantum Chemical Calculations on Peptides. *J. Phys. Chem. B* **2001**, *105*, 6474–6487.

(52) Perdew, J. P.; Burke, K.; Ernzerhof, M. Generalized Gradient Approximation Made Simple. *Phys. Rev. Lett.* **1996**, *77*, 3865–3868.

(53) Grimme, S. Semiempirical GGA-type Density Functional Constructed With a Long-range Dispersion Correction. *J. Comput. Chem.* **2006**, *27*, 1787–1799.

(54) Ditchfield, R.; Hehre, W. J.; Pople, J. A. Self Consistent Molecular–Orbital Methods. IX. An Extended Gaussian–Type Basis for Molecular-Orbital Studies of Organic Molecules. *J. Chem. Phys.* **1971**, *54*, 724–728.

(55) Frisch, M. J.; Trucks, G. W.; Schlegel, H. B.; Scuseria, G. E.; Robb, M. A.; Cheeseman, J. R.; Scalmani, G.; Barone, V.; Mennucci, B.; Petersson, G. A.; *et al.*, Gaussian09 Revision D.01. Gaussian Inc. Wallingford CT 2013.

(56) Maier, J. A.; Martinez, C.; Kasavajhala, K.; Wickstrom, L.; Hauser, K. E.; Simmerling, C. ff14SB: Improving the Accuracy of Protein Side Chain and Backbone Parameters from ff99SB. *J. Chem. Theory Comput.* **2015**, *11*, 3696–3713.

(57) Case, D. A.; Betz, R. M.; Botello-Smith, W.; Cerutti, D. S.; Cheatham, T. E.; Darden, T.; Duke, R. E.; Giese, T. J.; Gohlke, H.; Goetz, A. W.; *et al.*, AMBER16. **2016**,

(58) Wang, J.; Wolf, R. M.; Caldwell, J. W.; Kollman, P. A.; Case, D. A. Development and Testing of a General AMBER Force field. *J. Comput. Chem.* **2004**, *25*, 1157–1174.

(59) Genheden, S.; Ryde, U. The MM/PBSA and MM/GBSA Methods to Estimate Ligand-binding Affinities. *Expert Opin. Drug Discov.* **2015**, *10*, 449–461.

(60) Johnson, E. R.; Keinan, S.; Mori-Sánchez, P.; Contreras-García, J.; Cohen, A. J.; Yang, W. Revealing Noncovalent Interactions. *J. Am. Chem. Soc.* **2010**, *132*, 6498–6506.

(61) Contreras-García, J.; Johnson, E. R.; Keinan, S.; Chaudret, R.; Piquemal, J.-P.; Beratan, D. N.; Yang, W. NCIPLOT: A Program for Plotting Noncovalent Interaction Regions. *J. Chem. Theory Comput.* **2011**, *7*, 625–632.

(62) Humphrey, W.; Dalke, A.; Schulten, K. VMD - Visual Molecular Dynamics. *J. Molec. Graphics,* **1996**, *14*, 33–38.

(63) Varshney, A.; Brooks, F. P.; Wright, W. V. Computing Smooth Molecular Surfaces. *IEEE Comput. Graph. Appl. Mag.* **1994**, *14*, 19–25.

(64) Klunk, W. E.; Lopresti, B. J.; Ikonomovic, M. D.; Lefterov, I. M.; Koldamova, R. P.; Abrahamson, E. E.; Debnath, M. L.; Holt, D. P.; Huang, G.-F.; Shao, L.; *et al.*, Binding of the Positron Emission Tomography Tracer Pittsburgh Compound-B Reflects the Amount of Amyloid-β in Alzheimer's Disease Brain But Not in Transgenic Mouse Brain. *J. Neurosci.* **2005**, *25*, 10598–10606.

(65) Leuma Yona, R.; Mazères, S.; Faller, P.; Gras, E. Thioflavin Derivatives as Markers for Amyloid-β Fibrils: Insights into Structural Features Important for High-Affinity Binding. *Chem. Med. Chem.* **2008**, *3*, 63–66.

(66) Lindberg, D. J.; Wranne, M. S.; Gatty, M. G.; Westerlund, F.; Esbjörner, E. K. Steady-state and Time-resolved Thioflavin-T Fluorescence Can Report on Morphological Differences in Amyloid Fibrils Formed by Aβ-(1-40) and Aβ(1-42). *Biochem. Biophys. Res. Commun.* **2015**, *458*, 418–423.

(67) Sulatskaya, A. I.; Kuznetsova, I. M.; Belousov, M. V.; Bondarev, S. A.; Zhouravleva, G. A.; Turoverov, K. K. Stoichiometry and Affinity of Thioflavin T Binding to Sup35p Amyloid Fibrils. *PLoS One.* **2016**, *11*, E0156314.

(68) Miller, Y.; Ma, B.; Nussinov, R. The Unique Alzheimers β-Amyloid Triangular Fibril Has a Cavity Along the Fibril Axis under Physiological Conditions. *J. Am. Chem. Soc.* **2011**, *133*, 2742–2748.

Graphical TOC Entry

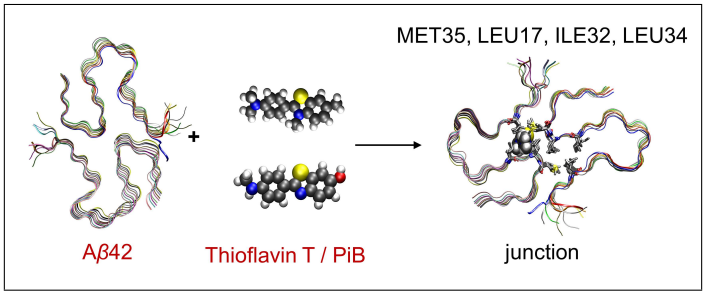

TOC Graphic